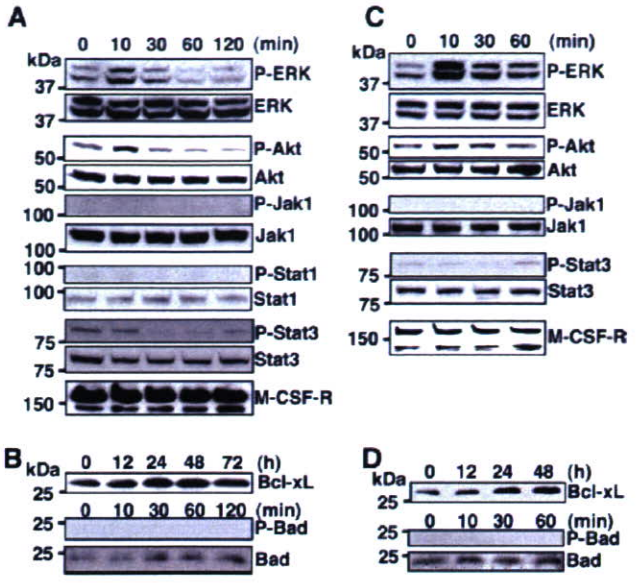

Figure 5. M-CSF activated ERK, Akt, and up-regulated Bcl-xL expression in differentiated H9c2 cells. H9c2 cardiomyocytes (**A** and **B**) or H9c2 myotubes (**C** and **D**) were stimulated with M-CSF (100 ng/ml) for the indicated time periods, and then the cell lysates were blotted with antibodies specific for the activated form of ERK (phospho-ERK), Akt (phospho-Akt), Jak1 (phospho-Jak1), Stat1 (phospho-Stat1), Stat3 (phospho-Stat3), or phosphorylated Bad (phospho-Bad). The membranes were reblotted with antibodies to total ERK, Akt, Jak1, Stat1, Stat3, or Bad, respectively. Expression of M-CSF-R or Bcl-xL was confirmed by blotting the membrane with specific antibodies. Similar results were obtained from three independent experiments.

(Figure 5C). M-CSF gradually up-regulated Bcl-xL expression until 48 hours (Figure 5D) but did not phosphorylate Bad at Ser112 (Figure 5D).

The Role of M-CSF-Induced Akt and ERK Activation in VEGF Production and Cell Survival in Differentiated H9c2 Cells

M-CSF increases VEGF production through Akt activation in skeletal muscles. To determine the role of Akt activation in H9c2 cardiomyocytes VEGF production, H9c2 cardiomyocytes were treated with Akt-specific inhibitor LY294002, and the culture supernatant was assayed by ELISA. LY294002 and M-CSF treatment for 2 days significantly impaired VEGF production in H9c2 cardiomyocytes (Figure 6A). LY294002 and M-CSF treatment for 3 days further decreased VEGF production, and the VEGF level became less than the detection level (Figure 6A). To determine the role of ERK and Akt activation after M-CSF treatment in differentiated H9c2 cell survival, differentiated H9c2 cells were treated with LY294002 or the ERK-specific inhibitor PD98059. PD98059 inhibited ERK activation and LY294002 inhibited Akt activation in H9c2 cardiomyocytes (Figure 6B). Similar results were obtained from H9c2 myotubes (data not shown). PD98059 enhanced H_2O_2-induced cell death of H9c2 cardiomyocytes (Figure 6C). The protective effect of M-CSF was impaired by PD98059; however, M-CSF significantly protected H9c2 cardiomyocytes from cell death (Figure 6C). A similar result was obtained from LY294002 in H9c2 cardiomyocytes (Figure 6C). In H9c2 myotubes, PD 98059 enhanced H_2O_2-induced cell death, and PD98059

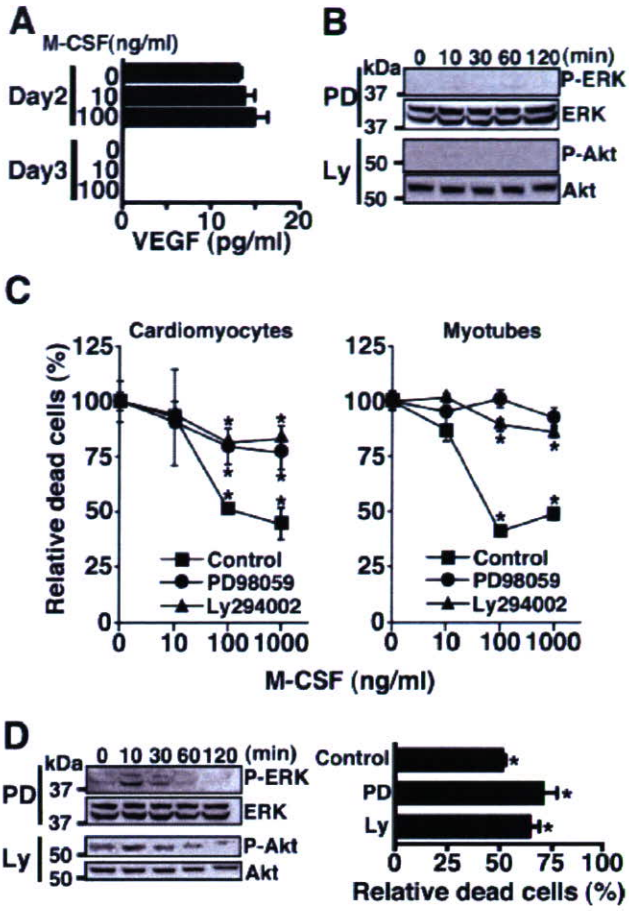

Figure 6. The role of M-CSF-induced Akt and ERK activation in VEGF production and cell protection in differentiated H9c2 cells. **A:** H9c2 cardiomyocytes were cultured with M-CSF and 10 μmol/L LY294002 for the indicated time periods. The culture medium was changed daily and ELISA determined the VEGF level. **B:** H9c2 cardiomyocytes were incubated with 30 μmol/L PD98059 (PD) or 10 μmol/L LY294002 (Ly) for 30 minutes, then stimulated with M-CSF (100 ng/ml) and inhibitors, and analyzed as described in Figure 5. **C:** Differentiated H9c2 cells were stimulated with indicated amount of M-CSF with PD98059 (30 μmol/L) or LY294002 (10 μmol/L) for 24 hours. Then the cells were stimulated with H_2O_2 (40 μmol/L) for 8 hours, and WST assay determined the dead cells. M-CSF (0 ng/ml) in each group is considered as 100%, and relative cell death rates in each group are shown. $^*P < 0.03$ compared with 0 ng/ml M-CSF in each group. Similar results were obtained from three independent experiments. **D:** H9c2 cardiomyocytes were incubated with reduced concentrations of PD98059 (6 μmol/L) or LY294002 (2 μmol/L). Left: H9c2 cardiomyocytes were treated with PD98059 or LY294002 for 30 minutes, stimulated with M-CSF (100 ng/ml) and inhibitors, and then analyzed as described in Figure 5. Right: H9c2 cardiomyocytes were treated with PD98059, LY294002, or without inhibitors (control) with (100 ng/ml) or without (0 ng/ml) M-CSF for 24 hours. Then the cells were stimulated with H_2O_2 (40 μmol/L) for 8 hours, and dead cells were assessed by WST assay. In each inhibitor group, dead cells at 0 ng/ml M-CSF are considered as 100%, and relative cell death rates at 100 to 0 ng/ml M-CSF in each inhibitor group are shown. $^*P < 0.02$ compared with 0 ng/ml M-CSF in each group.

abolished the protective effect of M-CSF (Figure 6C). LY294002 enhanced H_2O_2-induced cell death in H9c2 myotubes; however, M-CSF significantly protected H9c2 myotubes from cell death (Figure 6C). Moreover, a dose-response experiment of PD98059 or LY294002 was performed to observe ERK or Akt phosphorylation and cellular survival of H9c2 cardiomyocytes (Figure 6D). Similar results were obtained from H9c2 myotubes (data not shown). VEGF protected myogenic cells from cell death.[34] To confirm whether the cell survival effect of M-CSF de-

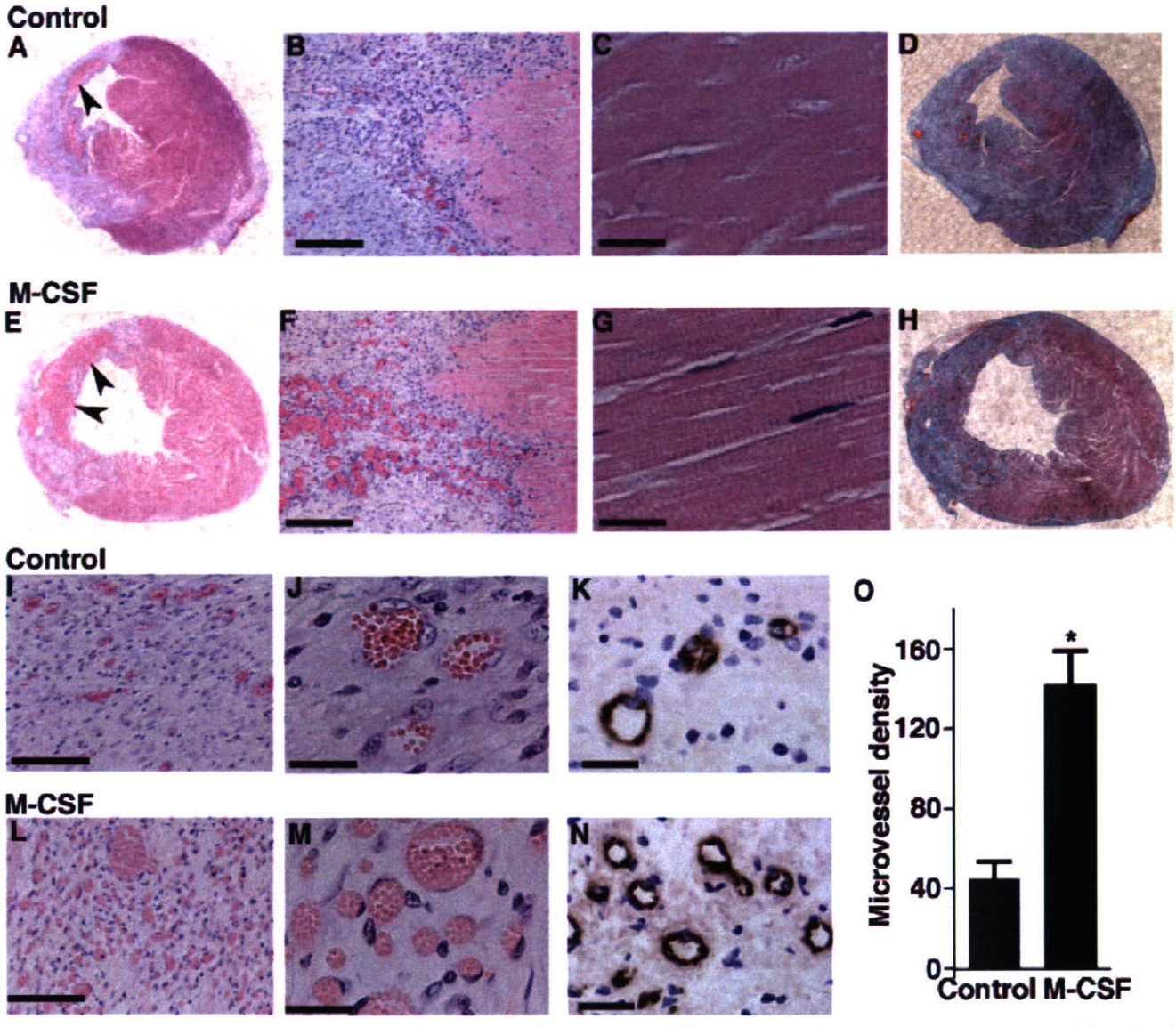

Figure 7. M-CSF promotes angiogenesis in goat heart after myocardial infarction. The goat left anterior descending coronary artery was permanently ligated, and the goats were sacrificed on day 14. M-CSF indicates goats intravenously injected with M-CSF shortly after the coronary artery ligation daily until day 13. Controls were injected with saline. Paraffin sections were stained with H&E (**A–C**, **E–G**, **I**, **J**, **L**, and **M**), Masson's elastic stain (**D** and **H**), and anti-factor VIII-related antigen antibody (**K** and **N**). **A** and **E:** Left anterior descending coronary artery ligation induced myocardial infarction. **Arrowheads** indicate cardiomyocytes in ischemic lesions. (**B**, **C**, **F**, and **G**) Microscopic observations indicated the cardiomyocytes in the ischemic lesions were dead. **D** and **H:** The green staining indicates fibrosis or scars in hearts. **I**, **J**, **L**, and **M:** The microvessels in ischemic lesions. **K** and **N:** The microvessels in ischemic lesions were immunohistochemically stained with anti-factor VIII-related antigen antibody. **O:** M-CSF significantly increased microvessel density in ischemic lesions ($^*P < 0.01$, $n = 3$ per group). The images represent one of three goats in each group. Scale bars: 200 μm (**B** and **F**); 20 μm (**C**, **G**, **J**, **K**, **M**, and **N**); 100 μm (**I** and **L**).

pends on VEGF, H9c2 cardiomyocytes and myotubes were cultured with an anti-VEGF antibody and M-CSF. Incubation with anti-VEGF antibody did not impair the cell protective effect of M-CSF from H_2O_2 stimulation suggesting that the effect of M-CSF was not VEGF-dependent (data not shown).

M-CSF Promotes Angiogenesis in Goat Ischemic Heart after Permanent Coronary Artery Ligation

M-CSF treatment elevated systemic VEGF level in mice from a nondetectable level to potentially therapeutic levels.[14,15] The cell protective and angiogenic effects of M-CSF *in vivo* were examined using goats as a large animal model for myocardial infarction. Large animal models are necessary for evaluating growth factor-induced therapeutic angiogenesis,[3] and we have used goats for developing artificial heart devices.[27] We induced myocardial infarction by permanent left anterior descending coronary artery ligation. The coronary artery ligation resulted in LV infarction (Figure 7, A, D, E, and H). Macroscopically, M-CSF seemed to promote cardiomyocyte cell survival in ischemic lesions in comparison to the controls (Figure 7, A and E; arrowheads). Microscopy indicated that cardiomyocytes in ischemic lesions were dead cells in the controls (Figure 7, B and C). At low magnification, M-CSF seemed to protect cardiomyocytes from cell death in ischemic lesions (Figure 7F). However,

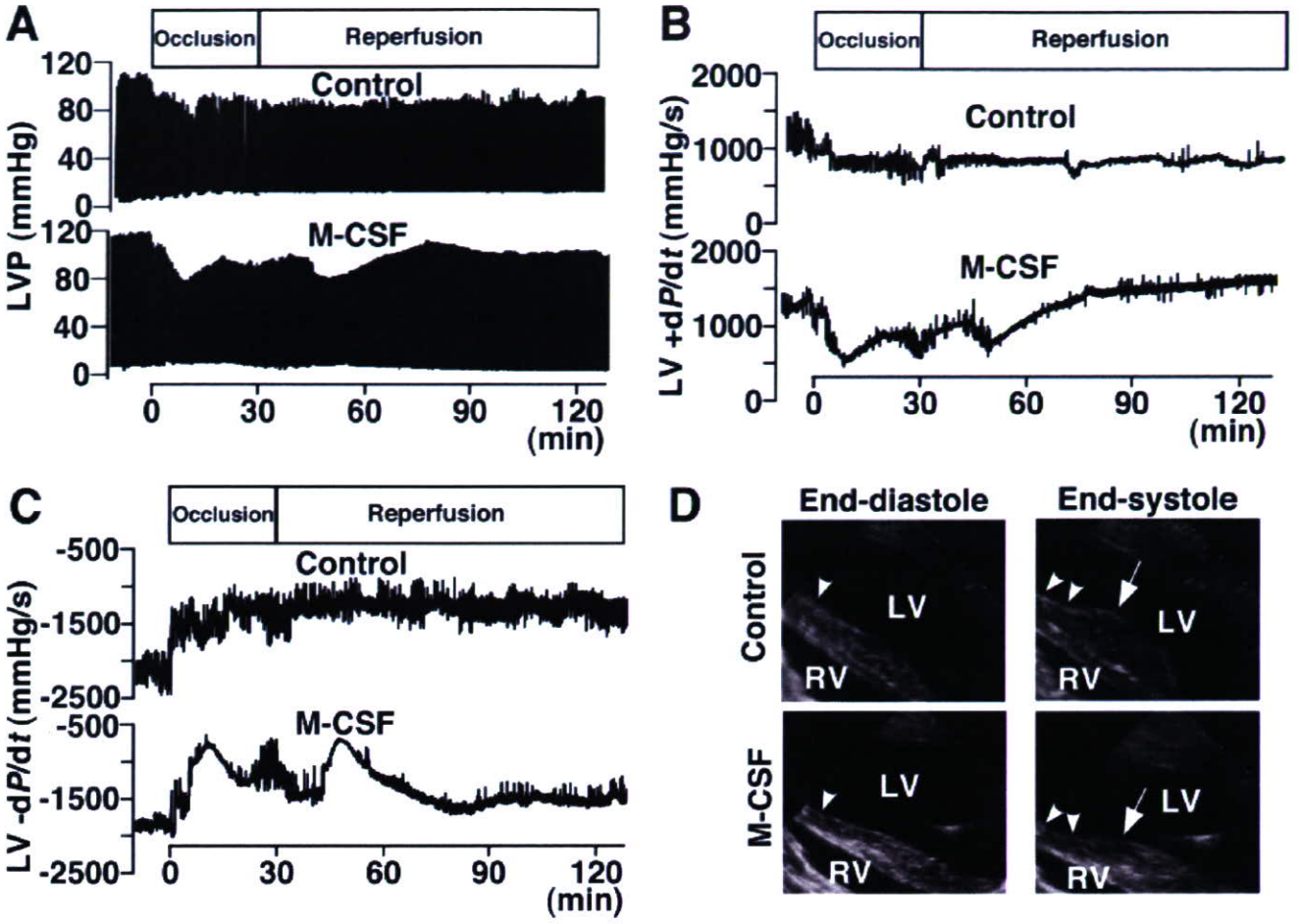

Figure 8. M-CSF pretreatment improved cardiac function after ischemic injury. M-CSF indicates goats intravenously injected with M-CSF daily for 3 days, whereas the control indicates goats injected with saline. The goat left anterior descending coronary artery was occluded for 30 minutes and then reperfused. **A–C:** Hemodynamic parameters before and during 30 minutes of left anterior descending coronary artery occlusion followed by 90 minutes of reperfusion are shown. Representative LVP records (**A**), representative positive dP/dt (**B**), and representative negative dP/dt (**C**) of control and M-CSF-treated goats. LVEDP, positive and negative dP/dt recovered in M-CSF-treated goats after reperfusion. **D: Arrowheads** indicate infarct areas. Compare **arrows**, which indicate wall contraction of nonischemic area at end systole, to **arrowheads**. In the infarct area, echocardiography shows dyskinetic wall movement in controls, whereas akinetic wall movement is shown in M-CSF-treated goats. Data are representative of three goats in each group.

at high magnification, most of the cardiomyocytes were dead (Figure 7G). Microvessels were observed in the ischemic lesions of control goats (Figure 7, I and J), and M-CSF treatment increased the number of microvessels (Figure 7, L and M). To confirm the microvessel density, we immunohistochemically stained goat hearts with anti-factor VIII-related antigen antibody (Figure 8, K and N).[23,24] M-CSF significantly increased microvessel density in ischemic lesions by 226% (Figure 7O). These results suggest that M-CSF promoted angiogenesis and induced collateral blood vessels in the ischemic heart. The infarct area quantification showed no significant difference between control and M-CSF-treated goats (controls, 30.4 ± 5.2%; M-CSF, 24.3 ± 2.1%). The residual presence of nuclei and cross striations in dead cardiomyocytes in ischemic lesions by M-CSF treatment (Figure 7G) suggests that the cardiomyocytes survived longer than control cardiomyocytes (Figure 7, C and G), but M-CSF-induced new vessels could not reach cardiomyocytes in ischemic lesions before their death.

M-CSF Pretreatment Improved Cardiac Function after Ischemic Injury Induced by Coronary Artery Occlusion-Reperfusion

Erythropoietin treatment did not change the infarct size, but it improved cardiac function in the rat coronary artery occlusion-reperfusion model.[5] Pretreatment with stem cell factor and G-CSF improved cardiac function after myocardial infarction.[7] To confirm further the effects of M-CSF in myocardial infarction, goats were pretreated with M-CSF for 3 days, and then myocardial infarction was induced by 30-minute left anterior descending coronary artery occlusion followed by reperfusion.[5,35] Cardiac function was assessed by measuring hemodynamic parameters using catheterization analysis and examining echocardiography. Echocardiographic examination showed no significant differences in basal findings in cardiac function in both groups. Catheterization analysis showed the LV pressure (LVP) records of control and M-CSF-treated goats (Figure 8A). LV end diastolic pressure

(LVEDP), which can influence overall cardiac function,[4] increased after the left anterior descending coronary artery occlusion in both groups. In controls, the LVEDP did not recover after reperfusion, but in M-CSF-treated goats, the LVEDP gradually recovered after reperfusion (Figure 8A), and at 90 minutes after the reperfusion, the LVEDP of M-CSF treated goats was significantly better than that of control goats (controls, 10.62 ± 0.98 mmHg; M-CSF, 7.61 ± 0.83 mmHg; $P < 0.02$). Positive and negative dP/dt are measures of overall cardiac contractility and relaxation, respectively.[4] Positive dP/dt decreased after the left anterior descending coronary artery occlusion both in control and M-CSF-treated goats (Figure 8B). After reperfusion, positive dP/dt did not recover in control goats (Figure 8B). In M-CSF treated goats, positive dP/dt gradually recovered after reperfusion and finally reached similar dP/dt levels before the occlusion (Figure 8B). At 90 minutes after the reperfusion, the positive dP/dt of M-CSF-treated goats was significantly better than that of control goats (controls, 886 ± 103 mmHg; M-CSF, 1506 ± 125 mmHg; $P < 0.01$). Moreover, recovery of negative dP/dt after left anterior descending coronary artery occlusion-reperfusion was observed only in M-CSF-treated goats (Figure 8C). At 90 minutes after the reperfusion, the negative dP/dt of M-CSF-treated goats was significantly better than that of control goats (controls, −1342 ± 92 mmHg; M-CSF, −1570 ± 108 mmHg; $P < 0.05$). Echocardiographic examination showed a paradoxical LV wall movement area indicated as a dyskinetic area after left anterior descending coronary artery occlusion in control goats (Figure 8D). In M-CSF-treated goats, echocardiography showed a LV wall movement arrest area indicated as an akinetic area after left anterior descending coronary artery occlusion, and a dyskinetic area could not be found (Figure 8D). In control hearts, the nonischemic wall contractions at end systole were enhanced. This suggested substitutive wall movement for the dyskinetic area to keep cardiac output (Figure 8D). These echocardiographic findings suggest improvement of LV wall movement in M-CSF-treated goats during left anterior descending coronary artery occlusion-reperfusion. The LV ejection fraction (LVEF) was evaluated by echocardiography, but LVEF did not significantly change between before and after the occlusion; therefore, LVEF between controls and M-CSF-treated ones were not compared. Recovery of LVEDP, positive and negative d*P*/d*t* after reperfusion, and improvement of LV wall movement during the left anterior descending coronary artery occlusion-reperfusion suggest M-CSF pretreatment improved cardiac function after ischemic injury.

Discussion

In this study, M-CSF increased VEGF production in hearts both *in vivo* and *in vitro*. *In vitro*, M-CSF increased VEGF production through Akt activation. Moreover, M-CSF directly protected cardiomyocytes from cell death by activating Akt and ERK resulting in up-regulation of the downstream anti-apoptotic protein Bcl-xL. M-CSF-R expression in the heart was shown both *in vivo* and *in vitro*, and these results suggest that the expression is functional. Similar cell-protective effects of M-CSF on H9c2 myotubes were shown. *In vivo*, M-CSF treatment after the onset of myocardial infarction promoted angiogenesis in the ischemic heart, suggesting development of collateral blood vessels. Furthermore, M-CSF pretreatment in the goat myocardial infarction model improves cardiac function, as indicated by improvement of LVEDP, positive and negative dP/dt, and LV wall movements.

Recent studies indicate intramyocardial transfer of plasmid or adenoviral DNA-encoding human VEGF has favorable effects in myocardial infarction animal models and in patients with coronary artery diseases.[1,2,36] Similar to these VEGF transfer strategies, M-CSF directly up-regulated VEGF production in cardiomyocytes. In addition, M-CSF significantly induced an increase in plasma VEGF in mice to therapeutic levels that induced therapeutic angiogenesis.[14,35] Therapeutic plasmid gene delivery to a target organ is difficult and often temporary. However, M-CSF treatment was easily achieved by peripheral intravenous or intramuscular injection. These data indicate a therapeutic potential of M-CSF in ischemic heart diseases. Basic fibroblast growth factor and hepatocyte growth factor have also been applied to therapeutic angiogenesis.[37] We treated mice with M-CSF and examined basic fibroblast growth factor and hepatocyte growth factor mRNA levels by quantitative RT-PCR. M-CSF did not increase basic fibroblast growth factor or hepatocyte growth factor mRNA levels in the heart (data not shown). We also examined plasma G-CSF level after M-CSF treatment in mice by ELISA. M-CSF did not increase plasma G-CSF level. However, there is still a possibility that M-CSF induces other factors that are responsible for the effects shown in this article.

Very recently, M-CSF was reported to accelerate infarct repair and attenuate LV dysfunction in rats.[35] However, these authors did not investigate VEGF induction or the cardioprotective effects of M-CSF and did not use a large animal model. In the present study, in the M-CSF-treated group, we observed an increase in microvessel density, increased presence of dead cardiomyocytes, and decreased presence of granuloma in ischemic lesions. The increased presence of dead cardiomyocytes in ischemic lesions and improvement of cardiac function after ischemia in M-CSF-treated goats suggest a longer survival of cardiomyocytes in M-CSF-treated goats than in the controls. This finding and the decreased presence of granuloma suggest that M-CSF reduced the progression rate of ischemic injury in ischemic hearts *in vivo*.

In human monocytes, LY294002 suppressed M-CSF-induced ERK activation.[38] This mechanism was explained as M-CSF stimulation-induced reactive oxygen species, which activated ERK. The addition of Akt inhibitor prevented reactive oxygen species production and thus suppressed ERK activation in M-CSF-stimulated monocytes.[38] In murine myeloid cell line FDC-P1, LY294002 suppressed M-CSF-induced ERK activation, but it was not significant.[39] In H9c2 cardiomyocytes, LY294002 seemed to impair ERK activation in part. To suggest the involvement of Akt in M-CSF-induced ERK

activation in cardiomyocytes, we may have to use other Akt-inhibiting methods, as this time we could not reach a clear conclusion. For VEGF production, PD98059 treatment for 1 day did not affect M-CSF-induced VEGF production in differentiated H9c2 cells, whereas LY294002 treatment impaired M-CSF-induced VEGF production, suggesting M-CSF-induced VEGF production in differentiated H9c2 cells were Akt-dependent. This is the first report that suggested the presence of signal transduction pathways in cardiomyocytes in response to M-CSF. Further experiments are required for pursuing the M-CSF-induced intracellular signaling pathways in cardiomyocytes or in myotubes.

Goat hearts have a left coronary artery-dominant blood supply.[40] The goat coronary artery anatomy was remarkably regular, and coronary artery collaterals could not be demonstrated,[40] indicating frailty after heart ischemic injury. For the left anterior descending coronary artery occlusion-reperfusion model, the goat left anterior descending coronary artery was ligated at a point ~40% from the beginning of the left coronary artery to the apex, but LVEF decrease could not be detected by echocardiography. Occlusion of a more proximal site of goat left anterior descending coronary artery has been reported to be invariably fatal,[40] and our preliminary experiments with a more proximal left anterior descending coronary artery ligation supported this finding. Therefore, using goats, LVEF after myocardial infarction could not be evaluated. We were not able to assess plasma VEGF and the involvement of bone marrow-derived cells in the goat model because the appropriate reagents are not commercially available. We could not find a staining method specific for cardiomyocyte viability in goat hearts. Infarct area quantification suggested a trend that M-CSF might decrease infarct area. However, infarct area quantification showed no significant difference in control and M-CSF-treated goat hearts. Further investigation is required to clarify the roles and mechanisms of M-CSF in ischemic diseases using other species and other M-CSF treatment protocols.

The cell-protective and VEGF-inducing effects of M-CSF both in cardiomyocytes and myotubes were shown, and the effects were confirmed by improvement of cardiac function and activated angiogenesis in goat ischemic hearts. M-CSF is already in use clinically, and data from patients such as side effects are accumulating. Moreover, M-CSF administration is easily performed with minimal invasiveness in human patients. In this study, we showed the potential benefits of M-CSF treatment and its new mechanisms in ischemic heart diseases.

Acknowledgments

We thank Peter Baluk, Hiroya Hashizume, Hiroshi Kubo, and Katsutoshi Nakayama for helpful comments on the manuscript; and Amy Ni and Shannon Freeman for correcting the manuscript.

References

1. Yoon YS, Johnson IA, Park JS, Diaz L, Losordo DW: Therapeutic myocardial angiogenesis with vascular endothelial growth factors. Mol Cell Biochem 2004, 264:63–74
2. Kastrup J, Jorgensen E, Ruck A, Tagil K, Glogar D, Ruzyllo W, Botker HE, Dudek D, Drvota V, Hesse B, Thuesen L, Blomberg P, Gyongyosi M, Sylven C: Direct intramyocardial plasmid vascular endothelial growth factor-A165 gene therapy in patients with stable severe angina pectoris A randomized double-blind placebo-controlled study: the Euroinject One trial. J Am Coll Cardiol 2005, 45:982–988
3. Markkanen JE, Rissanen TT, Kivela A, Yla-Herttuala S: Growth factor-induced therapeutic angiogenesis and arteriogenesis in the heart-gene therapy. Cardiovasc Res 2005, 65:656–664
4. Parsa CJ, Matsumoto A, Kim J, Riel RU, Pascal LS, Walton GB, Thompson RB, Petrofski JA, Annex BH, Stamler JS, Koch WJ: A novel protective effect of erythropoietin in the infarcted heart. J Clin Invest 2003, 112:999–1007
5. Calvillo L, Latini R, Kajstura J, Leri A, Anversa P, Ghezzi P, Salio M, Cerami A, Brines M: Recombinant human erythropoietin protects the myocardium from ischemia-reperfusion injury and promotes beneficial remodeling. Proc Natl Acad Sci USA 2003, 100:4802–4806
6. Harada M, Qin Y, Takano H, Minamino T, Zou Y, Toko H, Ohtsuka M, Matsuura K, Sano M, Nishi J, Iwanaga K, Akazawa H, Kunieda T, Zhu W, Hasegawa H, Kunisada K, Nagai T, Nakaya H, Yamauchi-Takihara K, Komuro I: G-CSF prevents cardiac remodeling after myocardial infarction by activating the Jak-Stat pathway in cardiomyocytes. Nat Med 2005, 11:305–311
7. Orlic D, Kajstura J, Chimenti S, Limana F, Jakoniuk I, Quaini F, Nadal-Ginard B, Bodine DM, Leri A, Anversa P: Mobilized bone marrow cells repair the infarcted heart, improving function and survival. Proc Natl Acad Sci USA 2001, 98:10344–10349
8. Miki T, Miura T, Nishino Y, Yano T, Sakamoto J, Nakamura Y, Ichikawa Y, Ikeda Y, Kobayashi H, Ura N, Shimamoto K: Granulocyte colony stimulating factor/macrophage colony stimulating factor improves postinfarct ventricular function by suppression of border zone remodelling in rats. Clin Exp Pharmacol Physiol 2004, 31:873–882
9. Ohno R, Miyawaki S, Hatake K, Kuriyama K, Saito K, Kanamaru A, Kobayashi T, Kodera Y, Nishikawa K, Matsuda S, Yamada O, Omoto E, Takeyama H, Tsukuda K, Asou N, Tanimoto M, Shiozaki H, Tomonaga M, Masaoka T, Miura Y, Takaku F, Ohashi Y, Motoyoshi K: Human urinary macrophage colony-stimulating factor reduces the incidence and duration of febrile neutropenia and shortens the period required to finish three courses of intensive consolidation therapy in acute myeloid leukemia: a double-blind controlled study. J Clin Oncol 1997, 15:2954–2965
10. Kawakami Y, Nagai N, Ohama K, Zeki K, Yoshida Y, Kuroda E, Yamashita U: Macrophage-colony stimulating factor inhibits the growth of human ovarian cancer cells in vitro. Eur J Cancer 2000, 36:1991–1997
11. Stanley ER, Berg KL, Einstein DB, Lee PS, Pixley FJ, Wang Y, Yeung YG: Biology and action of colony-stimulating factor-1. Mol Reprod Dev 1997, 46:4–10
12. Giordano FJ, Gerber HP, Williams SP, VanBruggen N, Bunting S, Ruiz-Lozano P, Gu Y, Nath AK, Huang Y, Hickey R, Dalton N, Peterson KL, Ross Jr J, Chien KR, Ferrara N: A cardiac myocyte vascular endothelial growth factor paracrine pathway is required to maintain cardiac function. Proc Natl Acad Sci USA 2001, 98:5780–5785
13. Maharaj AS, Saint-Geniez M, Maldonado AE, D'Amore PA: Vascular endothelial growth factor localization in the adult. Am J Pathol 2006, 168:639–648
14. Okazaki T, Ebihara S, Takahashi H, Asada M, Kanda A, Sasaki H: Macrophage colony-stimulating factor induces vascular endothelial growth factor production in skeletal muscle and promotes tumor angiogenesis. J Immunol 2005, 174:7531–7538
15. Kalka C, Masuda H, Takahashi T, Gordon R, Tepper O, Gravereaux E, Pieczek A, Iwaguro H, Hayashi SI, Isner JM, Asahara T: Vascular endothelial growth factor$_{165}$ gene transfer augments circulating endothelial progenitor cells in human subjects. Circ Res 2000, 86:1198–1202
16. Kallies A, Rosenbauer F, Scheller M, Knobeloch KP, Horak I: Accumulation of c-Cbl and rapid termination of colony-stimulating factor 1 receptor signaling in interferon consensus sequence bind-

ing protein-deficient bone marrow-derived macrophages. Blood 2002, 99:3213–3219
17. Novak U, Harpur AG, Paradiso L, Kanagasundaram V, Jaworowski A, Wilks AF, Hamilton JA: Colony-stimulating factor 1-induced STAT1 and STAT3 activation is accompanied by phosphorylation of Tyk2 in macrophages and Tyk2 and JAK1 in fibroblasts. Blood 1995, 86:2948–2956
18. Kelley TW, Graham MM, Doseff AI, Pomerantz RW, Lau SM, Ostrowski MC, Franke TF, Marsh CB: Macrophage colony-stimulating factor promotes cell survival through Akt/protein kinase B. J Biol Chem 1999, 274:26393–26398
19. Ménard C, Pupier S, Mornet D, Kitzmann M, Nargeot J, Lory P: Modulation of L-type calcium channel expression during retinoic acid-induced differentiation of H9C2 cardiac cells. J Biol Chem 1999, 274:29063–29070
20. van den Eijnde SM, van den Hoff MJ, Reutelingsperger CP, van Heerde WL, Henfling ME, Vermeij-Keers C, Schutte B, Borgers M, Ramaekers FC: Transient expression of phosphatidylserine at cell-cell contact areas is required for myotube formation. J Cell Sci 2001, 114:3631–3642
21. Kang YJ, Zhou ZX, Wang GW, Buridi A, Klein JB: Suppression by metallothionein of doxorubicin-induced cardiomyocyte apoptosis through inhibition of p38 mitogen-activated protein kinases. J Biol Chem 2000, 275:13690–13698
22. Okazaki T, Sakon S, Sasazuki T, Sakurai H, Doi T, Yagita H, Okumura K, Nakano H: Phosphorylation of serine 276 is essential for p65 NF-κB subunit-dependent cellular responses. Biochem Biophys Res Commun 2003, 300:807–812
23. Seno H, Oshima M, Ishikawa TO, Oshima H, Takaku K, Chiba T, Narumiya S, Taketo MM: Cyclooxygenase 2- and prostaglandin E_2 receptor EP_2-dependent angiogenesis in $Apc^{\Delta 716}$ mouse intestinal polyps. Cancer Res 2002, 62:506–511
24. Bildfell RJ, Valentine BA, Whitney KM: Cutaneous vasoproliferative lesions in goats. Vet Pathol 2002, 39:273–277
25. Ebihara S, Guibinga GH, Gilbert R, Nalbantoglu J, Massie B, Karpati G, Petrof BJ: Differential effects of dystrophin and utrophin gene transfer in immunocompetent muscular dystrophy (mdx) mice. Physiol Genomics 2000, 3:133–144
26. Sakon S, Xue X, Takekawa M, Sasazuki T, Okazaki T, Kojima Y, Piao JH, Yagita H, Okumura K, Doi T, Nakano H: NF-κB inhibits TNF-induced accumulation of ROS that mediate prolonged MAPK activation and necrotic cell death. EMBO J 2003, 22:3898–3909
27. Wang Q, Yambe T, Shiraishi Y, Duan X, Nitta S, Tabayashi K, Umezu M: An artificial myocardium assist system: electrohydraulic ventricular actuation improves myocardial tissue perfusion in goats. Artif Organs 2004, 28:853–857
28. Kim WG, Cho SR, Sung SH, Park HJ: A chronic heart failure model by coronary artery ligation in the goat. Int J Artif Organs 2003, 26:929–934
29. Eubank TD, Galloway M, Montague CM, Waldman WJ, Marsh CB: M-CSF induces vascular endothelial growth factor production and angiogenic activity from human monocytes. J Immunol 2003, 171:2637–2643
30. Ide H, Seligson DB, Memarzadeh S, Xin L, Horvath S, Dubey P, Flick MB, Kacinski BM, Palotie A, Witte ON: Expression of colony-stimulating factor 1 receptor during prostate development and prostate cancer progression. Proc Natl Acad Sci USA 2002, 99:14404–14409
31. Baines CP, Molkentin JD: STRESS signaling pathways that modulate cardiac myocyte apoptosis. J Mol Cell Cardiol 2005, 38:47–62
32. Valks DM, Cook SA, Pham FH, Morrison PR, Clerk A, Sugden PH: Phenylephrine promotes phosphorylation of Bad in cardiac myocytes through the extracellular signal-regulated kinases 1/2 and protein kinase A. J Mol Cell Cardiol 2002, 34:749–763
33. Matsui T, Rosenzweig A: Convergent signal transduction pathways controlling cardiomyocyte survival and function: the role of PI 3-kinase and Akt. J Mol Cell Cardiol 2005, 38:63–71
34. Arsic N, Zacchigna S, Zentilin L, Ramirez-Correa G, Pattarini L, Salvi A, Sinagra G, Giacca M: Vascular endothelial growth factor stimulates skeletal muscle regeneration in vivo. Mol Ther 2004, 10:844–854
35. Yano T, Miura T, Whittaker P, Miki T, Sakamoto J, Nakamura Y, Ichikawa Y, Ikeda Y, Kobayashi H, Ohori K, Shimamoto K: Macrophage colony-stimulating factor treatment after myocardial infarction attenuates left ventricular dysfunction by accelerating infarct repair. J Am Coll Cardiol 2006, 47:626–634
36. Rutanen J, Rissanen TT, Markkanen JE, Gruchala M, Silvennoinen P, Kivela A, Hedman A, Hedman M, Heikura T, Orden MR, Stacker SA, Achen MG, Hartikainen J, Yla-Herttuala S: Adenoviral catheter-mediated intramyocardial gene transfer using the mature form of vascular endothelial growth factor-D induces transmural angiogenesis in porcine heart. Circulation 2004, 109:1029–1035
37. Azuma J, Taniyama Y, Takeya Y, Iekushi K, Aoki M, Dosaka N, Matsumoto K, Nakamura T, Ogihara T, Morishita R: Angiogenic and antifibrotic actions of hepatocyte growth factor improve cardiac dysfunction in porcine ischemic cardiomyopathy. Gene Ther 2006, 13:1206–1213
38. Bhatt NY, Kelley TW, Khramtsov VV, Wang Y, Lam GK, Clanton TL, Marsh CB: Macrophage-colony-stimulating factor-induced activation of extracellular-regulated kinase involves phosphatidylinositol 3-kinase and reactive oxygen species in human monocytes. J Immunol 2002, 169:6427–6434
39. Gobert Gosse S, Bourgin C, Liu WQ, Garbay C, Mouchiroud G: M-CSF stimulated differentiation requires persistent MEK activity and MAPK phosphorylation independent of Grb2-Sos association and phosphatidylinositol 3-kinase activity. Cell Signal 2005, 17:1352–1362
40. Lipovetsky G, Fenoglio JJ, Gieger M, Srinivasan MR, Dobelle WH: Coronary artery anatomy of the goat. Artif Organs 1983, 7:238–245

ARTICLE IN PRESS

Available online at www.sciencedirect.com

ScienceDirect

Ultrasonics xxx (2007) xxx–xxx

Ultrasonics

www.elsevier.com/locate/ultras

Fractal dimension of 40 MHz intravascular ultrasound radio frequency signals

E. Santos Filho [a,*], Y. Saijo [a], A. Tanaka [b], T. Yambe [a], M. Yoshizawa [c]

[a] *Department of Medical Engineering and Cardiology, Institute of Development, Aging, and Cancer, Tohoku University, 4-1 Seiryomachi, Aoba-ku, Sendai 980-8575, Japan*

[b] *Faculty of Symbiotic Systems Science, Fukushima University, Japan*

[c] *Information Synergy Center, Tohoku University, Japan*

Received 18 April 2007; received in revised form 24 August 2007; accepted 24 August 2007

Abstract

Objective: Fully automatic tissue characterization in intravascular ultrasound systems is still a challenge for the researchers. The present work aims to evaluate the feasibility of using the Higuchi fractal dimension of intravascular ultrasound radio frequency signals as a feature for tissue characterization.

Methods: Fractal dimension images are generated based on the radio frequency signals obtained using mechanically rotating 40 MHz intravascular ultrasound catheter (Atlantis SR Plus, Boston Scientific, USA) and compared with the corresponding correlation images.

Conclusion: An inverse relation between the fractal dimension images and the correlation images was revealed indicating that the hard or slow moving tissues in the correlation image usually have low fractal dimension and vice-versa. Thus, the present study suggests that fractal dimension images may be used as a feature for intravascular ultrasound tissue characterization and present better resolution then the correlation images.

PACS: 87.62; 87.59.M; 47.53.+n

Keywords: Intravascular ultrasound; Tissue characterization; Fractal dimension; Radio frequency signal; Coronary artery

1. Introduction

Intravascular ultrasound (IVUS) has been clinically applied since early 1990s. The tomographic orientation of ultrasound enables visualization of the entire circumference of the vessel wall and provide information about tissues beneath the luminal border. However, visual analysis of IVUS images by experts is usually accompanied by limitations associated with interpersonal variations, errors due to fatigue, environmental distractions, etc. Computer-aided tissue characterization of IVUS images has a potential to add objective strength to the interpretation of the expert becoming an important tool for coronary diseases diagnosis. Analysis of IVUS radio frequency (RF) signal has potential to provide powerful features for tissue characterization because it is the original source of information from the backscattered ultrasound beam.

Nair et al. [1] successfully used spectral analysis of backscattered IVUS RF signals to classify plaque composition by constructing classification trees. However, for test data, in spite of presenting accuracy of 100% for calcified-necrosis, the accuracies for fibrolipid and collagen were 83% and 69%, respectively, showing that improvements and new signal processing techniques are still necessary for a full tissue characterization in IVUS imaging.

Signal processing based on estimating fractal dimension in a time series has been successfully applied in a number of

* Corresponding author. Tel.: +81 22 717 8517; fax: +81 22 717 8518.
E-mail address: esmeraldo@ieee.org (E.S. Filho).

0041-624X/$ - see front matter © 2007 Elsevier B.V. All rights reserved.
doi:10.1016/j.ultras.2007.08.006

Please cite this article in press as: E.S. Filho et al., Fractal dimension of 40 MHz intravascular ultrasound radio ..., Ultrasonics (2007), doi:10.1016/j.ultras.2007.08.006

medical applications due to its capability of expressing signal irregularity [1–5].

Alacam et al. [6] showed that the features obtained by statistical modeling of RF echo can be used as decision criterion for tissue characterization in breast cancer diagnosis. They proposed the fractional differencing auto regressive moving average (FARMA) model which captures the fractal and long term correlated nature of the backscattered speckle texture. Using a linear classifier their method presented an area of 0.87 under the receiver operating characteristic (ROC) curve.

Moradi et al. [7] have presented an innovative approach for detection of prostate cancer based on the fractal analysis of RF ultrasound echo signals. They used Higuchi's [8] method to calculate the fractal dimension over a region of interest (ROI) and used it as feature to detect the prostate cancer through a Bayesian classifier [9]. Their algorithm presented accuracy of 86% indicating the feasibility of their approach.

Saijo et al. [10,11], have developed a method for tissue characterization based on two-dimensional correlation between two consecutive frames of an IVUS sequence. This technique was shown capable of distinguishing regions of fast moving fluid like blood or surrounding tissue from region of slow moving or stable like the vessel wall.

In this work, we investigate the feasibility of using the Higuchi's fractal dimension as a feature for tissue characterization in IVUS through comparison with correlation images.

2. Materials and methods

IVUS data were acquired with an IVUS console Clear View Ultra (Boston Scientific Inc., Natick-MA, USA) and 40 MHz mechanically rotating IVUS catheter Atlantis SR Plus (Boston Scientific Inc., Natick-MA, USA) and the pulse repetition rate was 7680 Hz. RF data were digitized and stored in a personal computer (PC) (Dell 8250, Pentium 4, 2.4 GHz, 1.50 GB RAM, Dell Inc., Round Rock, TX, USA) using an A/D board GAGE Compuscope 8500 (500 Msamples/s, with 8 bits of resolution, Gage Applied Inc., Montreal, Quebec, Canada) for off-line analysis. The algorithms were developed using MATLAB (The Mathworks Inc., Natick, MA, USA). A single frame of the IVUS system consisted of 256 lines so that 7680 pulses made 30 frames per second (f/s). RF signal data were acquired in vivo from 14 human left anterior descending (LAD) coronary arteries during percutaneous transluminal coronary angioplasty (PTCA). The patients average age was 72 ± 12 years and six of them presented detected calcification regions and one detected soft plaque in their IVUS images. This process was approved by a local investigation review board and was performed in accordance with the ethical principles for medical research involving human subjects. We obtained written informed consent from all the subjects.

2.1. Fractal dimension image

The concept of fractal dimension is based on the property of self-similarity. In spite of not being self-similar over all the scales, the IVUS RF signals usually present some level of self-similarity within some range and thus the Higuchi fractal dimension can be used as an efficient method to express the irregularity of the RF signals in the ROIs of appropriate size.

Higuchi's algorithm [8] is proven to be a stable method to estimate the fractal dimension of a time series and, more importantly, works well for time series with few samples. The algorithm, computes mean length of the signal at different scales, plots a log–log graph of length versus scale and measures the slope of the linear fit of this graph as the fractal dimension.

Thus, for generation of the fractal dimension images the following algorithm was used.

Algorithm. For each ROI defined by the position of a 100 points wide sliding window, the following steps were used:

1. Extract the signal envelop through the calculation of the absolute value of the Hilbert transform.
2. Normalize the envelop by dividing it by its maximum value in that sample.
3. Calculate the fractal dimension of the normalized signal using the Higuchi method.
4. The sliding window is shifted of 25 points and the above steps are repeated for all RF lines that comprise the IVUS image.

2.2. Correlation image

Conventional B-mode IVUS images were generated from RF signals by software developed by our group [10]. Then the IVUS image was divided into 64×64 square shape ROIs. Template matching method was applied for calculation of correlation and displacement of the ROIs between the consecutive two frames. Template matching is the process of determining the presence and the location of a reference image or an object inside a scene image under analysis by a spatial cross-correlation process. Fig. 1 shows the schematic illustration of template matching method. If the coordinates of the center of the ROI in the first frame (a) are defined as $p(0,0)$ and the most similar patterned ROI in the next frame (b) is $q(k,l)$, the correlation is given by:

$$R_{fg}(k,l) = \frac{\sum_{i=0}^{n^2-1}(f_i - \bar{f}_i)(g_i - \bar{g}_i)}{\sqrt{\sum_{i=0}^{n^2-1}(f_i - \bar{f}_i)^2 \sum_{i=0}^{n^2-1}(g_i - \bar{g}_i)^2}} \quad (1)$$

where f_i and g_i are pixels inside the ROI in consecutive frames, $\bar{f}_i$ and $\bar{g}_i$ are the corresponding mean gray level values of each ROI, and n is the length of the side of the square shaped ROI.

Please cite this article in press as: E.S. Filho et al., Fractal dimension of 40 MHz intravascular ultrasound radio ..., Ultrasonics (2007), doi:10.1016/j.ultras.2007.08.006

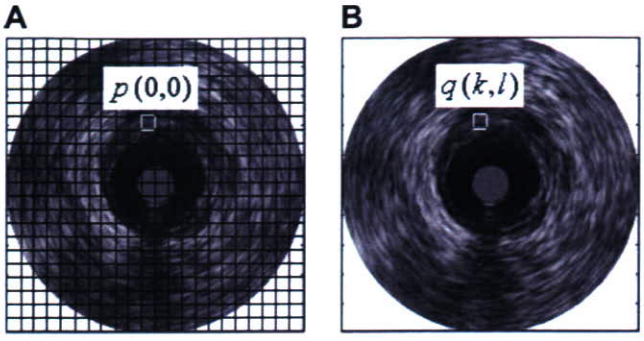

Fig. 1. Schematic illustration of template matching method. The coordinates of the center of the ROI in the first frame (A) is defined as $p(0, 0)$ and the most similar ROI in the next frame (B) is $q(k, l)$.

Based on our tests, we could observe that the moving regions such as blood and surrounding tissues presented correlation values below 0.5 and the regions of vessel wall presented correlation values above 0.75. The vessel wall was assumed stable during 1/30 s.

3. Results

In Fig. 2, we can see an example of two samples of IVUS RF signal extracted from the region of blood and the region of vessel wall. It can be seen that the sample extracted from the blood region presents a more irregular shape than the sample from the region of vessel. As the fractal dimension can be regarded as a measure of irregularity, we used the fractal dimension as a feature for tissue characterization.

In Fig. 3C and F, we can see two examples of fractal dimension images. They are images whose pixel colors represent the fractal dimension of a 100 points wide sliding window centered at the corresponding position in the RF line. In spite of being quite noisy, we can observe that the regions of lumen present fractal dimension values higher (light blue and green) than the vessel wall region (dark blue). More homogeneous regions, like calcification regions for example, present a lower fractal dimension value (dark blue).

Also, in Fig. 3B and E, we can compare the fractal images with the correlation images, which are images whose pixel value represents the correlation index calculated through Eq. (1). The correlation image shows its lowest level in the regions of blood (light blue), which is the most dynamic region. This fact is also detected through the fractal dimension image.

In Fig. 3A, we can observe clearly the boundary lumen/vessel that is confirmed in Fig. 3B, where the lumen region presents correlation values usually below 0.5, represented by light green or light blue, due to the fast moving blood. The red region is the static or slow moving vessel wall. In the fractal dimension image (Fig. 3C) we can observe that

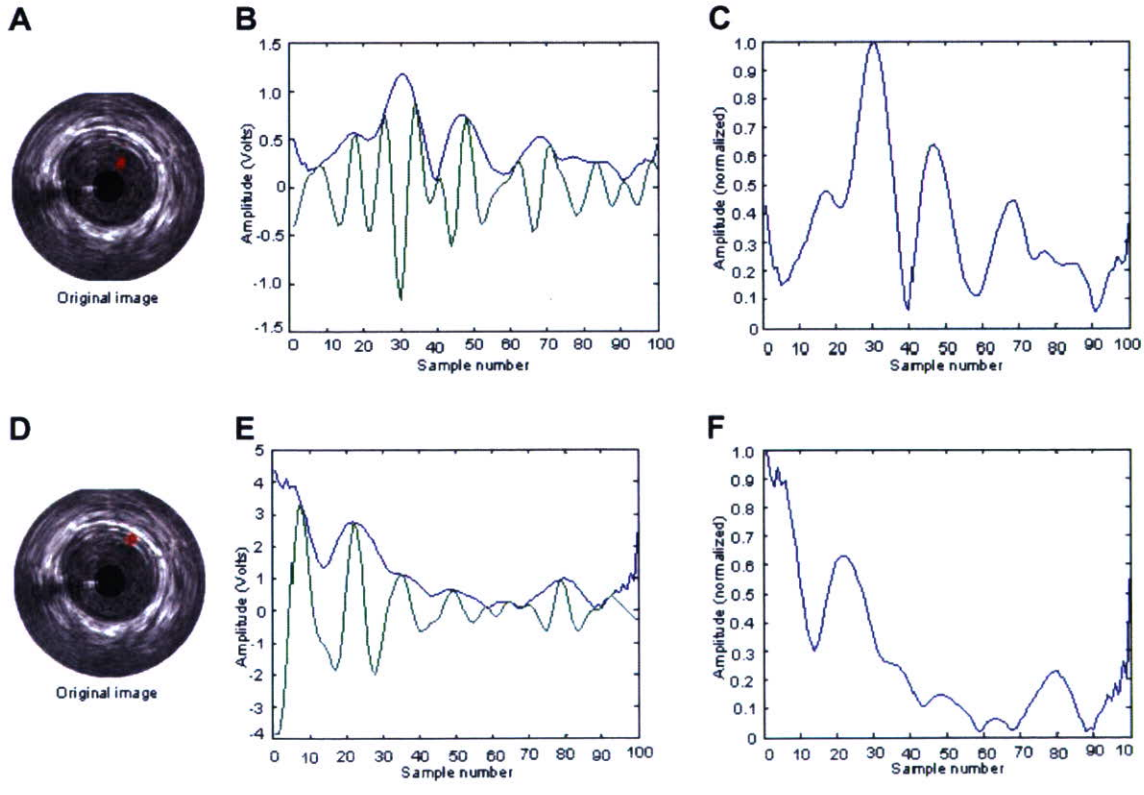

Fig. 2. Example of RF signal ROIs extracted from lumen region (A) and vessel wall region (D). The small regions in red in (A) and (D) indicate the position from where the ROIs were extracted. They are 100 samples length ROIs. (B) and (E) are the graphs of the RF signals ROIs (in green) and their respective envelop (in blue). (C) and (F) are graphs of the normalized envelops.

Please cite this article in press as: E.S. Filho et al., Fractal dimension of 40 MHz intravascular ultrasound radio ..., Ultrasonics (2007), doi:10.1016/j.ultras.2007.08.006

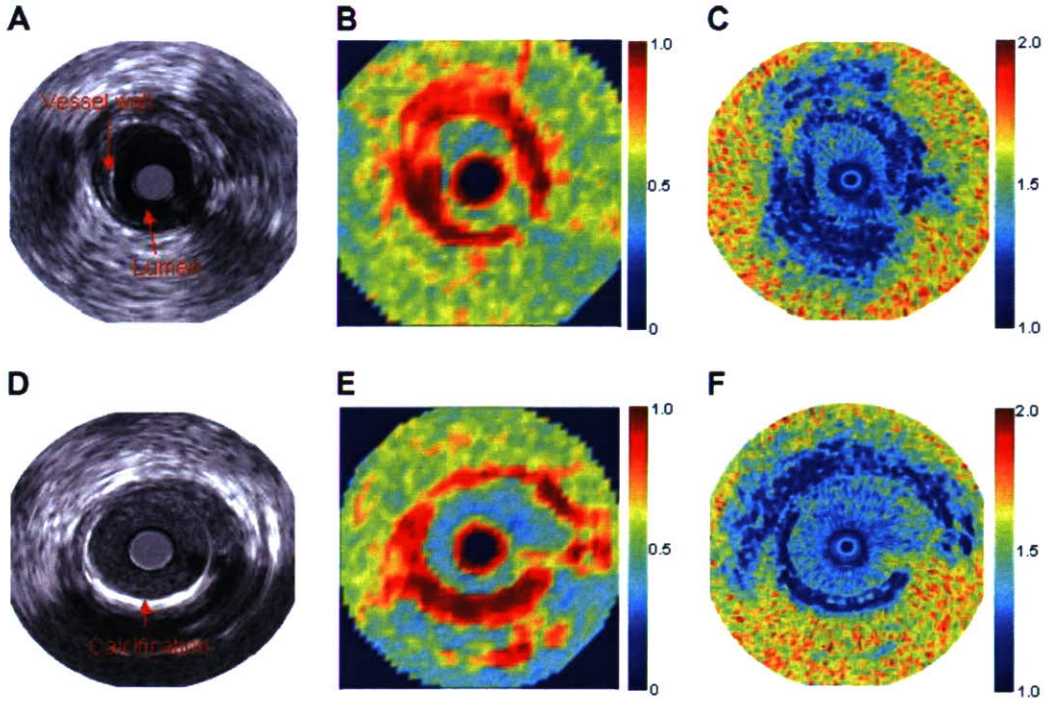

Fig. 3. Comparison between correlation image and fractal dimension image. (A) and (D) are the original images. (B) and (E) are examples of correlation images. (C) and (F) are example of fractal dimension images.

the lumen region is light blue whereas the vessel wall region is dark blue. This means that the fractal dimension in the lumen region, usually between 1.25 and 1.5, is higher than the fractal dimension in the vessel wall region that is usually below 1.20. This suggests that the irregularity level of the RF signal expressed by Higuchi fractal dimension can be used, to some extent, to characterize the moving tissues. The region outside the vessel in Fig. 3C is quite yellow and red, with fractal dimension values around 1.7, mainly because this is a region of high noise level. The corresponding area in Fig. 3B present low correlation level indicating fast moving connecting tissues. Additionally, we can observe in Fig. 3E and F that the region of calcium is also a region of high correlation value and low fractal dimension. It can also be observed that the fractal dimension images present better resolution than the correlation images.

4. Discussion

The examples in Fig. 2 showed that, besides the differences in amplitude, the irregularity of the envelop is fairly different in these both regions suggesting that a measure of signal irregularity could be a useful discriminator for regions of vessel wall and lumen. Saijo et al. [10] have observed similar results through the two-dimensional correlation analysis. Their results were validated by comparisons with histology data.

Accordingly to our tests, RF signal samples shorter then 60 points did not provide acceptable results because the images generated using a window of this width did not present clear contrast between the lumen and the vessel wall. The highest contrast is achieved for sliding window with width of around 100 points. Sliding windows wider than 100 points did not present visible improvements.

As reported in [8], the Higuchi method presented more stable results when compared with other methods based on power spectrum. In tests performed with IVUS RF signals the power spectrum based fractal dimension did not provide satisfactory results, probably, due to the large amount of noise, suggesting the robustness of Higuchi method.

Using the PC described in Section 2, the average processing time needed to generate the fractal dimension images was 128 s. This suggests that the proposed algorithm may be used in real time if more powerful hardware is used and the program is optimized.

The fractal dimension images presented an average contrast-to-noise ratio (CNR) of 3.73 whereas the correlation image presented 3.05. However, together with lower CNR, the correlation images present lower resolution. Thus the fractal images with a CNR of 3.05 seen to present a satisfactory trade-off between noise and resolution because the resultant fractal dimension images presented less distortion of the lumen contour than the correlation images as can be seen in Fig. 3.

Comparing images from different patients, for example, patients with calcification and patients without calcification, we could observe that the fractal dimension values in the calcification regions is similar to levels presented in the vessel wall region, as shown in Fig. 3. This

Please cite this article in press as: E.S. Filho et al., Fractal dimension of 40 MHz intravascular ultrasound radio ..., Ultrasonics (2007), doi:10.1016/j.ultras.2007.08.006

suggests that the fractal dimension images may not be useful in calcification detection. In tests with image containing soft plaque, the resulting fractal dimension image did not present clear contrast between the soft plaque and blood. Thus, this method does not seem likely to be a good discriminator for plaques. However, it may be useful as a pre-processing stage toward luminal contour detection.

5. Conclusion

A comparison between correlation images and fractal dimension images was presented and we could observe that, in general, the regions of high correlation values in the correlation image correspond to the regions of low fractal dimension in the corresponding fractal dimension image and vice-versa. This fact suggests that the fractal dimension, as measure of irregularity of the RF echo signal, can be also an indicator of the moving characteristic of the interrogated tissue as well as the correlation image. However, the fractal dimension image has the advantage of presenting more clearly the fine details of the luminal contour when compared to the correlation images.

Acknowledgement

This study was supported by the Grants-in-Aid from the Ministry of Health, Labor and Welfare of Japan (H17-nano-001).

References

[1] A. Nair, B.D. Kuban, N. Obuchowski, D.G. Vince, Assessing spectral algorithms to predict atherosclerotic plaque composition with normalized and raw intravascular ultrasound data, Ultrasound in Medicine and Biology 27 (2001) 1319–1331.

[2] R. Jennane, W.J. Ohley, S. Majumdar, G. Lemineur, Fractal analysis of bone X-ray tomographic microscopy projections, IEEE Transactions on Medical Imaging 20 (2001) 443–449.

[3] T. Stosic, B.D. Stosic, Multifractal analysis of human retinal vessels, IEEE Transactions on Medical Imaging 25 (2006) 1101–1107.

[4] P. Asvestas, S. Golemati, G.K. Matsopoulos, K.S. Nikita, A.N. Nicolaides, Fractal dimension estimation of carotid atherosclerotic plaques from b-mode ultrasound: a pilot study, Ultrasound in Medicine and Biology 28 (2002) 1129–1136.

[5] W.L. Lee, Y.C. Chen, K.S. Hsieh, Ultrasonic liver tissues classification by fractal feature vector based on m-band wavelet transform, IEEE Transaction on Medical Imaging 22 (2003) 382–392.

[6] B. Alacam, B. Yazici, N. Bilgutay, F. Forsberg, C. Piccoli, Breast tissue characterization using modeling of ultrasonic RF echo, Ultrasound in Medicine and Biology 30 (2004) 1397–1407.

[7] M. Moradi, P. Ablmaesumi, P.A. Isolato, D.R. Siemens, E.E. Sauerbrei, P. Mousavi. A new feature for detection of prostate cancer based in RF ultrasound echo signals, in: Proceedings of IEEE Ultrasonics Symposium, 2006. pp. 2084–2087.

[8] T. Higuchi, Approach to an irregular time series on the basis of the fractal theory, Physica D 31 (1988) 277–283.

[9] R.M. Rangayyan, Biomedical Image Analysis, CRC Press, Boca Raton, FL, USA, 2005, pp. 1118.

[10] Y. Saijo, A. Tanaka, T. Iwamoto, E. Santos Filho, M. Yoshizawa, A. Hirosaka, M. Kijima, Y. Akino, Y. Hanadate, T. Yambe, Intravascular two-dimensional tissue strain imaging, Ultrasonics 44 (2006) e147–e151.

[11] Y. Saijo, A. Tanaka, N. Owada, Y. Akino, S. Nitta, Tissue velocity imaging of coronary artery by rotating-type intravascular ultrasound, Ultrasonics 42 (2004) 753–757.

Please cite this article in press as: E.S. Filho et al., Fractal dimension of 40 MHz intravascular ultrasound radio ..., Ultrasonics (2007), doi:10.1016/j.ultras.2007.08.006

ELSEVIER

Ultrasound in Med. & Biol., Vol. 34, No. 1, pp. 160–165, 2008

0301-5629/08/$–see front matter

doi:10.1016/j.ultrasmedbio.2007.06.025

● *Technical Note*

DETECTION AND QUANTIFICATION OF CALCIFICATIONS IN INTRAVASCULAR ULTRASOUND IMAGES BY AUTOMATIC THRESHOLDING

E. SANTOS FILHO,* Y. SAIJO,* A. TANAKA,† and M. YOSHIZAWA‡

*Department of Medical Engineering and Cardiology, Institute of Development, Aging, and Cancer, Tohoku University, Sendai; †Faculty of Symbiotic Systems Science, Fukushima University, Fukushima; and ‡Information Synergy Center, Tohoku University, Sendai, Japan

(*Received* 18 *January* 2007, *revised* 18 *May* 2007, *in final form* 26 *June* 2007)

Abstract—An innovative application of automatic thresholding is used for the detection of calcification regions in intravascular ultrasound images. *A priori* knowledge of the acoustic shadow that usually accompanies calcification regions is used to discriminate these from other bright regions in the image. A method for the calculation of the angle of calcification has also been developed. The proposed algorithms are applied to *in-vivo* images obtained from left anterior descending coronary arteries during percutaneous transluminal coronary angioplasty (n = 14). The resulting specificity is 72% and the sensitivity 84%. The receiver operating characteristic curve, the area under the curve being equal to 0.91, is plotted to evaluate the algorithm performance. (E-mail: esmeraldo@ieee.org) **© 2007 World Federation for Ultrasound in Medicine & Biology.**

Key Words: **Image segmentation, Calcification detection, Automatic thresholding.**

INTRODUCTION

It is estimated that cardiovascular diseases cause one-third of all deaths globally. Coronary artery disease is a chronic disease in which the coronary arteries gradually harden and narrow in a process called atherosclerosis. As the heart muscle is fed with oxygen-rich blood delivered by the coronary arteries, a blockage in these arteries can cause a heart attack (WHO 2005).

Currently, several imaging modalities are available to support the diagnosis of coronary artery diseases. X-ray coronary angiography and intravascular ultrasound (IVUS) are examples of the most commonly used diagnostic tools. Intravascular ultrasound has several important advantages over angiography and provides new diagnostic and therapeutic insights into coronary disease. The tomographic orientation of ultrasound enables visualization of the entire circumference of the vessel wall and provides information about the tissues beneath the luminal border (Kaneda et al. 2003).

As presented in the work of Rao et al. (2005), the knowledge about the origin and progression of atherosclerosis has advanced greatly in the last years. However, the factors that determine atheromatous plaque instability are not well understood. New diagnostic and therapeutic methods would have to be developed if an accurate and reliable prediction of plaque vulnerability were available. Based on histologic analysis of aortas with areas of gross atherosclerosis, Rao et al. (2005) observed that plaque instability is highly correlated with intraplaque hemorrhage, lipid content and plaque size. Calcification does not seem to be a significant indicator of plaque instability.

However, the amount of coronary calcium has been shown to be very important for physicians. Shaw et al. (2006) have conducted a study that confirms the prior findings that the prevalence of coronary calcification increases with age. They evaluated a unique method whereby estimates of the extent of coronary calcification may be used to adjust a patient's age. It was revealed by their study that for elderly patients with low-risk calcium scores, survival is equivalent to that for patients 1 to 10 years younger. On the other hand, for younger patients with moderate- to high-risk calcium scores, survival is equivalent to that for patients approximately 20 years older. Thus, a score that includes coronary calcium and age may be useful for prevention strategies.

Address correspondence to: E. Santos Filho, Department of Medical Engineering and Cardiology, Institute of Development, Aging, and Cancer, Tohoku University, 4–1 Seiryomachi, Aoba-ku, Sendai 980–8575, Japan. E-mail: esmeraldo@ieee.org

The presence or absence of calcium demonstrated by IVUS has been shown to be an important determinant of transcatheter interventional success (Scott et al. 2000). In theory, there may be a critical quantity of calcium that is predictive of an unsatisfactory outcome with balloon angioplasty, but without an accurate method to quantify coronary calcification, that critical calcium content cannot be determined.

Several studies on IVUS image segmentation have been published that aim to automate this process (Saijo et al. 2004, 2006a; Sonka et al. 1995; Brusseau et al. 2004; Vince et al. 2000).

In this paper, we present an algorithm based on automatic thresholding for the automatic detection of the calcification regions in IVUS images, which may be used for the automation of the method proposed by Scott et al. (2000).

MATERIALS AND METHODS

Intravascular ultrasound data were acquired with an IVUS console (Clear View Ultra, Boston Scientific Inc., Natick, MA, USA) and a 40-MHz mechanically rotating IVUS catheter (Atlantis SR Plus, Boston Scientific Inc.). Radiofrequency (RF) data were digitized and stored on a personal computer (Dell Precision Workstation 330, Dell Inc., Round Rock, TX, USA) using an A/D board (GAGE Compuscope 8500, 500 Msamples/s, 8-bit resolution, Gage Applied Inc., Montreal, Quebec, Canada) for off-line analysis. The images used were of the Windows bitmap type and the algorithms were developed using MATLAB (The Mathworks, Inc., Natick, MA, USA).

Subsequently, the RF signal was preprocessed and converted to a conventional B-mode IVUS image through a software developed by our group. Using this procedure we could remove the influence of the control settings of the IVUS console that usually affect algorithms based on image gray levels.

Radiofrequency signal data were acquired *in vivo* from 14 human left anterior descending (LAD) coronary arteries during percutaneous transluminal coronary angioplasty (PTCA). This process was approved by a local investigation review board and was performed in accordance with the ethical principles for medical research involving human subjects. We obtained written informed consent from all subjects.

Multithresholding segmentation

Calcification regions are usually very bright regions in IVUS images. Tests using speed of sound microscopy (Saijo et al. 2006b) have confirmed that the strongest echo is produced between calcium and lumen or calcium and media, where the difference in the specific acoustic impedance is large.

Thus, it is natural to consider thresholding as a simple method to segment calcification regions. However, in spite of being brighter compared with normal tissue, the gray levels of the calcified regions and normal tissue usually change from image to image. This fact makes it very difficult to determine a single threshold value capable of accurately segmenting a series of images.

Thus, it is necessary to adapt the threshold level for each input image. In this work, we used the Otsu method (Otsu 1979) to automatically find the optimal threshold for each image. However, in our tests, applying thresholding only once was not sufficient to obtain segmented regions that were reasonably close to the regions of calcification.

To solve this problem, a multithresholding method was applied, using successive applications of the Otsu method as summarized in the following algorithm. The Otsu method is summarized in the Appendix.

Algorithm 1. Step 1: Compute the histogram.

Step 2: Compute the optimal threshold k^* that maximizes the between-class variance $\sigma_B^2(k)$.

$\sigma_B^2(k^*) = \max\sigma_B^2(k)$

Step 3: Compute a new histogram for $i \geq k^*$.

Step 4: Go to step 2.

After several tests, it was observed that three iterations of the above algorithm were sufficient to obtain segmentation sufficiently close to the regions of calcification.

However, often normal tissue, parts of the catheter and artifacts also form very bright regions and may be wrongly segmented. For this reason, it is necessary to develop a method to ignore segmented bright regions that are not calcifications.

Identification of calcification from the regions-of-interest

Another characteristic of calcification regions is that they are usually accompanied by an acoustic shadow as a result of the high reflection of the ultrasound beam at such sites. Thus, an effective way to detect whether a given segmented bright region, hereafter called a region-of-interest (ROI), is a calcification region, is through the analysis of the region behind the ROI. In Fig. 1, there is an example of an IVUS image with a calcification region and a graph of the median gray level of the pixels in each column of the corresponding polar coordinate system image.

We can observe in Fig. 1 that the region of calcification is accompanied by an acoustic shadow, and the corresponding region in the graph presents a lower median level.

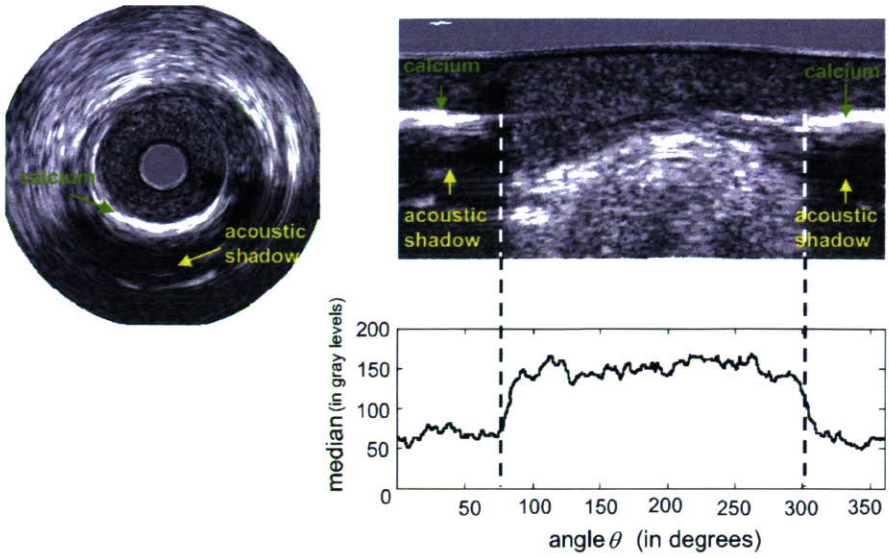

Fig. 1. Example of an IVUS image with a calcification and its corresponding graph of median gray level of the pixels in each column of the rectangular coordinates system corresponding to the original polar system of IVUS images.

Detection of acoustic shadow

To detect the acoustic shadow and then determine whether a given ROI is a calcification, the following algorithm is used:

Algorithm 2. Step 1: Determine the centroid of the segmented ROI.

Step 2: From the centroid of the ROI to the bottom of the image (pixels of the yellow line in Fig. 2), calculate the median gray-level value, *Med*.

Step 3: If $\frac{Med}{M_{cent}} \leq T_{med}$, then classify the ROI as a calcification. Otherwise, classify the ROI as a noncalcification region. M_{cent} denotes the gray level of the pixel at the centroid of the ROI.

T_{med} was chosen based on tests using several images. As illustrated in Fig. 2, only ROI 2 was selected as a calcification region because of its detected acoustic shadow.

The true-positive rate and the false-positive rate depend on the threshold value T_{med} used to define positive and negative test results. As we shift T_{med} in the range of the possible values of $\frac{Med}{M_{cent}}$ found in our tests (from 0.3 to 0.98), the true-positive rate and false-positive rate also present increasing values, which are used to construct the ROC curve. Some values are shown in Fig. 5 as examples.

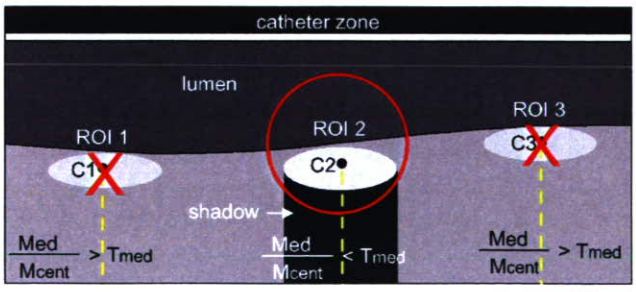

Fig. 2. Example of identification of calcification due to acoustic shadow. The ROI 1 and ROI 2 were not classified as calcification (indicated by the red X). The ROI 2 was classified as calcification (indicated by the red circle). The criterion for classification was the presence of acoustic shadow detected through analysis of the pixels in the yellow line. ROI = region of interest; C = centroid.

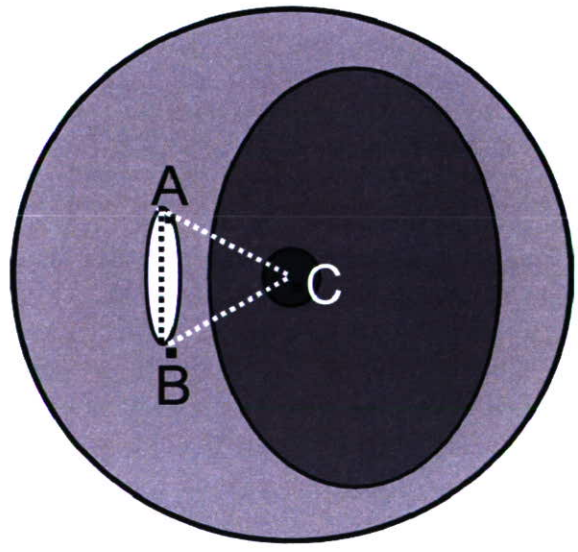

Fig. 3. Example of determination of the angle of calcification. (A) and (B) are the extreme points of the calcification region. (C) is the center of the catheter.

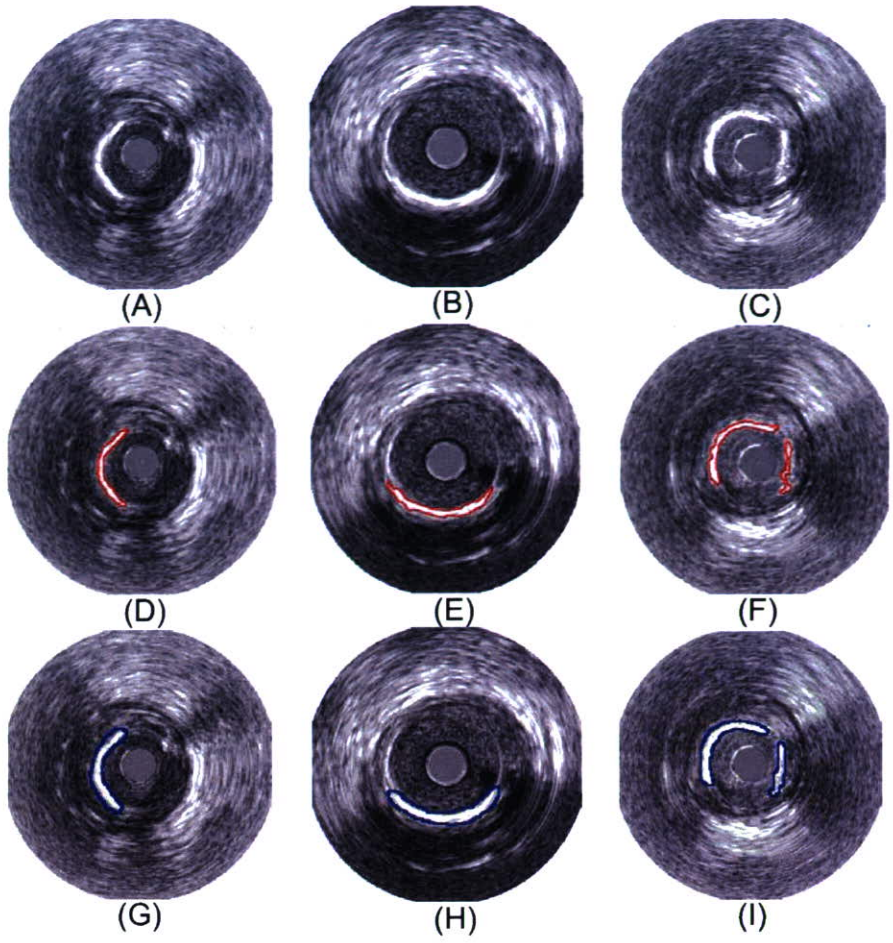

Fig. 4. Example of calcification regions automatically segmented. (A, B, C) Original images. (D, E, F) Corresponding automatically segmented images. (G, H, I) Corresponding manually segmented images. The outlined areas are the calcification regions.

Quantification of calcification regions

Usually, the method used to quantify calcium through IVUS images is based on the arc of calcium measured in a single frame of the IVUS movie of the site of the calcification. However, the accuracy of this method would be increased if it could take into account the extent of the total epicardial coronary calcium (Scott et al. 2000).

Scott et al. (2000) have proposed a method for calcification quantification similar to Simpson's rule, which is used in calculus to determine volumes. As a sequence of known areas separated by a known distance can be used to calculate volume, a sequence of known circumferences separated by a known distance can be used to calculate the surface area.

As the manual measurement of calcification across a sequence of frames is a tedious and time-consuming task, we developed an algorithm for the measurement of the angle of the calcification regions detected through the automatic thresholding. This method is summarized in the following algorithm:

Algorithm 3. Step 1: Determine the extreme points of the calcification region denoted by the letters A and B, as shown in Fig. 3.

Step 2: Determine the center of the image (center of the catheter), denoted by the letter C, and then calculate the length of the sides of the triangle determined by points A, B and C.

Step 3: Using the sine and cosine rules, calculate the angle whose vertex is at point C; this will be considered as the calcification angle.

Intravascular ultrasound sequences containing calcification regions were selected by an expert medical doctor, and from each calcification region sequence, one representative frame was selected for the tests. Then, the selected images were manually segmented by the expert medical doctor and used as our gold standard.

RESULTS

Using the algorithms for automatic thresholding and acoustic shadow detection, tests were performed and

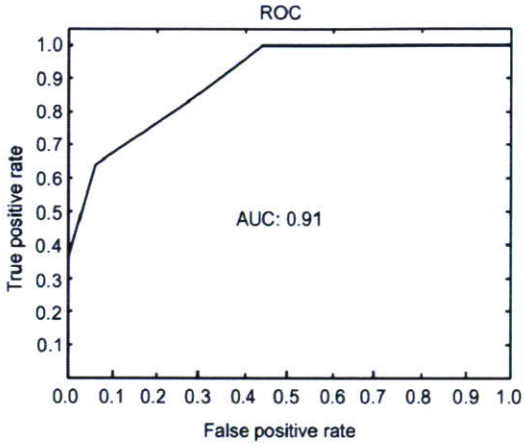

Example of ROC curve points

threshold	TPR	FPR
0.3	0.36 (9/25)	0.0 (0/18)
0.4	0.64 (16/25)	0.06 (1/18)
0.5	1.0 (25/25)	0.44 (8/18)

Fig. 5. Receiver operating characteristic curve. The AUC is equal to 0.91. TPR = true-positive rate; FPR = false-positive rate.

some of the results are shown in Fig. 4. We observe that in these images, the regions of calcification are segmented accurately. The threshold level used for the median values is empirically determined as $T_{med} = 0.45$. Table 1 summarizes the results of the tests, and the ROC curve is plotted in Fig. 5. The area under the curve (AUC) is equal to 0.91. The resulting specificity is 72% and the sensitivity 84%.

DISCUSSION

The analysis of the images in the rectangular coordinate system (demodulate RF line) corresponding to the originally polar system of the IVUS images facilitates the process of acoustic shadow detection because in the rectangular images, the shadow region is confined to a given number of columns, forming a rectangular area that can be scanned easily.

Sometimes part of the catheter may appear very bright and simultaneously present an acoustic shadow because of the presence of the guide wire. In such cases, part of the catheter may be wrongly segmented as a calcification. To prevent this problem, a test is performed to determine whether the centroid of the ROI is inside the 30-pixel-length radius circle centered at the catheter center. This circle corresponds, approximately, to the catheter region. Thus, if a ROI centroid falls inside this circle, it will not be considered as a candidate calcification region. However, because of this constraint, an underestimation of the amount of calcium may occur in the case of a highly concave calcification region that is very close to the catheter, causing its centroid to fall inside the catheter region. In this case, this calcification will not be detected. However, in our tests we did not find such a case.

Table 1. Table of results

	ROIs correctly classified	ROIs wrongly classified	Total number of ROIs
Calcification	21	4	25
Normal tissue	13	5	18

ROI = Region-of-interest.

The number of iterations of successive thresholding was determined empirically. It was observed that after each threshold, the value of the standard deviation of the gray level in the remaining regions usually declines. This information may be used to define a stopping criterion and then improve the robustness of the proposed algorithm.

In frames without calcification regions, the ROIs remaining after the third thresholding are usually very few in number and very small in size. Furthermore, in these images, the gray level declines smoothly away from the ROI. Thus, the gray level at the centroid of these ROIs and the gray levels in their neighborhood are usually very close; this makes the value $\frac{Med}{M_{cent}}$ approach unity and cause the ROIs to be classified as noncalcification regions.

The results were evaluated through visual inspection by the expert who also traced the manually segmented contours. In spite of some differences between the areas of the ROIs manually and automatically traced, the results were considered accurate because the parameter to be quantified was the length of the arc of the segmented calcification. The thickness of the segmented region was ignored because the ultrasound beam is almost completely reflected at the surface of the calcification regions and causes a shadow that makes it difficult to assess the real thickness of the calcification.

The false positives were caused by the presence of the guide-wire shadow. However, it is possible that regions of fibrosis may also be sufficiently bright compared with other tissues to cause $\frac{Med}{M_{cent}} \leq 0.45$ and be wrongly considered as calcifications. However, in our tests we did not find such a case.

The center of the vessel is the point that should be used for the calculation of the angle of the calcification. However, to find this center, it would be necessary to first accurately find the luminal contour. In our tests, the center of the image was used as an approximation of the center of the vessel.

As future work, the proposed algorithm may be combined with other existing methods for luminal contour segmentation, becoming an important step toward the full automation of the method proposed by Scott et al. (2000).

Acknowledgements—This study was supported by the Grants-in-aid from the Ministry of Health, Labour and Welfare of Japan (H17-nano-001).

REFERENCES

Brusseau E, Korte CL, Mastik F, Schaar J, van der Steen AFW. Fully automatic luminal contour segmentation in intracoronary ultrasound imaging—A statistical approach. IEEE Trans Med Imaging 2004;23:554–566.

Kaneda H, Honda Y, Yock PG, Fitzgerald PJ. What do cardiologists want from vascular ultrasound. In: Saijo Y, van der Steen AFW,eds. Vascular Ultrasound. Tokyo: Springer-Verlag, 2003:3–27.

Otsu N. A threshold selection method from gray-level histograms. IEEE Trans Systems Man Cybernectics 1979;9:62–66.

Rao DS, Goldin JG, Fishbien MC. Determinants of plaque instability in atherosclerotic vascular disease. Cardiovasc Pathol 2005;14:285–293.

Saijo Y, Tanaka A, Owada N, Akino Y, Nitta S. Tissue velocity imaging of coronary artery by rotating-type intravascular ultrasound. Ultrasonics 2004;42:753–757.

Saijo Y, Tanaka A, Iwamoto T, et al. Intravascular two-dimensional tissue strain imaging. Ultrasonics 2006a;44:e147–151.

Saijo Y, Hozumi N, Lee C, et al. Ultrasonic speed microscopy for imaging of coronary artery. Ultrasonics 2006b;44:e51–55.

Scott DS, Arora UK, Farb A, Virmani R, Weissman NJ. Pathologic validation of a new method to quantify coronary calcific deposits in vivo using intravascular ultrasound. Am J Cardiol 2000;85:37–40.

Shaw LJ, Raggi P, Berman DS, Callister TQ. Coronary artery calcium as a measure of biologic age. Atherosclerosis 2006;188:112–119.

Sonka M, Zhang X, Siebes M, et al. Segmentation of intravascular ultrasound images: A knowledge-based approach. IEEE Trans Med Imaging 1995;14:719–732.

Vince D, Dixon K, Cothren R, Cornhill J. Comparison of texture analysis methods for characterizations of coronary plaques in intravascular ultrasound images. Comput Med Imaging Graph 2000; 24:221–229.

World Health Organization. Cardiovascular diseases. Available at: http://www.who.int/topics/cardiovascular_diseases/en/. Accessed June 11, 2005.

APPENDIX

Automatic threshold estimator

Otsu (1979) developed an optimal threshold selection method based on the maximization of the separability of the resultant classes. His procedure is very effective and utilizes only the 0^{th} and first-order cumulative moments of the gray-level histogram. Thus, because of its simplicity and effectiveness, the Otsu method was used as the threshold estimator in this work.

Following Otsu's formulation, let the pixels of a given image be represented in L gray levels [1, 2, ···, L]. The number of pixels at gray level i is denoted by n_i and the total number of pixels by $N = n_1 + n_2 + \cdots + n_L$. After normalization, the gray-level histogram may be regarded as a probability distribution:

$$p_i = n_i/N \tag{1}$$

$$p_i \geq 0, \sum_{i=1}^{L} p_i = 1 \tag{2}$$

We separate the pixels into two classes, C_0 and C_1 (background and object or *vice versa*), by a threshold at gray level k; C_0 denotes pixels with gray levels [1, ···, k] and C_1 denotes pixels with levels [k + 1, ···, L]. Then, the probabilities of class occurrence and the class mean gray levels, respectively, are given by:

$$\omega_0 = \Pr(C_0) = \sum_{i=1}^{k} p_i = \omega(k) \tag{3}$$

$$\omega_1 = \Pr(C_1) = \sum_{i=k+1}^{L} p_i = 1 - \omega(k) \tag{4}$$

and

$$\mu_0 = \sum_{i=1}^{k} i\Pr(i|C_0) = \sum_{i=1}^{k} ip_i/\omega_0 = \mu(k)/\omega(k) \tag{5}$$

$$\mu_1 = \sum_{i=k+1}^{L} i\Pr(i|C_1) = \sum_{i=k+1}^{L} ip_i/\omega_1 = \frac{\mu_T - \mu(k)}{1 - \omega(k)}, \tag{6}$$

where

$$\omega(k) = \sum_{i=1}^{k} p_i \tag{7}$$

and

$$\mu(k) = \sum_{i=1}^{k} p_i \tag{8}$$

are the 0^{th} and first-order cumulative moments of the histogram up to the k^{th} level, respectively, and

$$\mu_T = \mu(L) = \sum_{i=1}^{L} ip_i \tag{9}$$

The optimal threshold is defined (Otsu 1979) as the value that maximizes the between-class variance

$$\sigma_B^2(k) = \frac{[\mu_T\omega(k) - \mu(k)]^2}{\omega(k)[1 - \omega(k)]} \tag{10}$$

Thus, the optimal threshold $k*$ is given by:

$$\sigma_B^2(k*) = \max_{1 \leq k < L} \sigma_B^2(k) \tag{11}$$